

Abila, A.L., et al., 2024, Strength of viscous subduction interfaces: A global compilation: Geology, <https://doi.org/10.1130/G52518.1>

Supplemental Material

Input parameters, source material, and implemented viscous rheologies for modeled shear zones.

Tables S1–S2

Figures S1–S2.14

Dataset

SUPPLEMENTAL MATERIAL

Methods

Choice of Flow Laws

The flow laws implemented (Table S2) were chosen as these experimentally-constrained flow laws are (1) applicable to high pressure conditions in the viscous interface and (2) best represent the dominant mineralogy/lithology of the reported rock units at high-pressure conditions.

However, it should be noted that recent works have shown abundant diffusion creep at high-pressure conditions for both mafic (e.g. Stunitz et al., 2020) and metasedimentary (e.g. Wassman and Stöckhert, 2013) lithologies. However, we lack diffusion parameters at high pressure conditions for non-schist lithologies, making dislocation creep flow laws the only viable solution. Theoretical pressure-solution creep models exist for schistose lithologies (e.g. Behr & Platt, 2013), but the parametrization of these flow laws are heavily debated and not yet experimentally determined, allowing for up to two orders of magnitude variations even for similar deformation conditions (see Condit et al., 2022 and Schmidt and Platt, 2022). Thus, it is unclear how these theoretical flow laws can be systematically applied to our collection of sections with variable schist characteristics.

Choice of Shear Zones

It should be noted that the shear zones chosen were mapped with enough resolution and clear boundaries as these are required to properly implement the strain rate across the shear zone. Numerous deep interface shear zones have been reported in literature, however they (1) lack resolution resolution (e.g. Sambagawa Metamorphic Belt (Takasu, 1984; Ota et al., 2004), Sanandaj-Sirjan Zone (Davoudian et al., 2008)), (2) have debated deformation evolution paths

(e.g. Ring Mountain (Wakabayashi, 2015)), (3) lack clear interface boundaries and/or estimated thicknesses (e.g. Sai-Hatat window (El-Shazly et al., 1997), Belomorian Mobile Belt (Shchipansky et al., 2012), Sistan mélange (Angiboust et al., 2013), Santa Elena serpentinite mélange (Escudé- Viruete & Baumgartner, 2014), Lago Superiore Unit (Locatelli et al., 2018), Catalina Schist (Hoover et al., 2022)), or a combination of the above factors. Thus, while these shear zones are well-studied, we cannot implement the model.

Strain Rate Calculations

The bulk shear strain rate implemented on the sections are derived using the convergence plate velocities from plate reconstructions of Merdith et al. (2021) and the thickness of section (Ly, see Table S1), as

$$\dot{\epsilon} = \frac{V_x}{L_y}$$

where $\dot{\epsilon}$ is the bulk shear strain rate, V_x is the convergence velocity, which set the top and bottom velocities, and L_y is the mapped thickness of the interface.

Governing Equations

The two-dimensional numerical code employs conservative finite differences on a fully staggered Eulerian grid and Lagrangian markers (Ruh et al., 2024). Governing equations include conservation of mass for incompressible media:

$$\frac{\partial u_i}{\partial u_j} = 0$$

and conservation of momentum:

$$\frac{-\partial P}{\partial u_i} + \frac{\partial \tau_{ij}}{\partial x_i} = 0$$

where P is dynamic stress, u_i and u_j are velocities, x_i are spatial coordinates, and τ_{ij} is the deviatoric stress tensor. The equations are discretized on a Eulerian grid to solve for velocity and pressure. Velocities are interpolated onto the Lagrangian markers following the fourth-order Runge-Kutta method.

A Maxwell visco-elastic relationship is implemented in the form:

$$\dot{\epsilon}_{ij} = \frac{1}{2\eta} \tau_{ij} + \frac{1}{2G} \frac{D_{cr}\tau_{ij}}{Dt}$$

where $\dot{\epsilon}_{ij}$ is the total deviatoric strain rate tensor, τ_{ij} is the deviatoric stress tensor, η is the effective viscosity, G is the elastic modulus, and $\frac{D_{cr}\tau_{ij}}{Dt}$ is the co-rotational time derivative, discretized using first-order finite differences.

Effective viscosity is computed independently from the power law relationship:

$$\eta = 0.5 \cdot \frac{1}{A f^r} \tau_{II}^{(1-n)} d^{-m} \exp\left(\frac{Q}{RT}\right)$$

where $\dot{\epsilon}$ is strain rate, A is the pre-exponential factor, and τ_{II} is the second invariant of the stress tensor from the previous timestep, given as

$$\tau_{II} = \sqrt{\frac{1}{2} \tau_{ij}^2}$$

The geometry and boundary conditions of the models are discussed in the main text. A schematic diagram of the set-up is shown in Fig. S3. The resolution of the models are dependent on the dimension of the source section, with Eulerian grid spacing set at ~ 0.05 - 0.1% of the thickness (Ly) of the section (see Table A1 for individual model dimensions). Timesteps are taken at 50% movement along x or y , with a maximum timestep of 100 years, until the model deforms for ~ 10 ky.

Results

To quantify the effect of block geometry and spatial distribution, synthetic models were used. These models were deformed with the same volumetric distribution (38% blocks, 62% matrix) and deformation conditions as the low-temperature equivalent of Model 5a (Tauern Window Eclogite Zone). Fig. S6A uses eclogite blocks in a quartz schist matrix, while Fig. A6B uses quartz schist blocks in an eclogite matrix. These models show the effect of (1) the size of the blocks (i.e. a higher number of blocks indicate a smaller average block size), (2) the clustering of blocks (i.e. more clusters indicate smaller clusters, while an even distribution will show no clustering), (3) the elongation of the blocks parallel to shear direction (i.e. the ratio of the length of the shear-parallel axis to the length of the shear-perpendicular axis of an ellipsoidal block), and (4) the eccentricity of the block parallel to shear (i.e. the amount of flattening parallel to shear). We observe that in a strong block-weak matrix scenario, typical of *mélanges*, the spatial distribution and geometry of lithologies present only varies the strength up to a factor of 1.5. In contrast, in a weak block-strong matrix scenario, e.g. serpentinite-bearing schistose *mélanges* and large-scale blueschist bodies, the weak blocks weaken the bulk strength by up to a factor of 5, indicative of the blocks accommodating a larger portion of the strain, in contrast to a strong block-weak matrix set-up, wherein the blocks accommodate minimal strain. These models show that the spatial distribution and geometry of the lithologies present contribute to the strength variations observed in the modelled sections.

Supplemental References

Andjić, G., Escuder-Viruete, J., Baumgartner-Mora, C., Baumgartner, P. O., Castillo-Carrión, M., & Gabites, J. (2019). Origin and geodynamic significance of the Siuna Serpentinite Mélange,

Northeast Nicaragua: Insights from the large-scale structure, petrology and geochemistry of the ultramafic blocks. *Lithos*, 340–341, 1–19. <https://doi.org/10.1016/j.lithos.2019.05.002>

Angiboust, S., Agard, P., De Hoog, J. C. M., Omrani, J., & Plunder, A. (2013). Insights on deep, accretionary subduction processes from the Sistan ophiolitic “mélange” (Eastern Iran). *Lithos*, 156–159, 139–158. <https://doi.org/10.1016/j.lithos.2012.11.007>

Angiboust, S., Agard, P., Glodny, J., Omrani, J., & Oncken, O. (2016). Zagros blueschists: Episodic underplating and long-lived cooling of a subduction zone. *Earth and Planetary Science Letters*, 443, 48–58. <https://doi.org/10.1016/j.epsl.2016.03.017>

Behr, W. M., & Platt, J. P. (2014). Brittle faults are weak, yet the ductile middle crust is strong: Implications for lithospheric mechanics. *Geophysical Research Letters*, 41(22), 8067–8075. <https://doi.org/10.1002/2014GL061349>

Condit, C. B., French, M. E., Hayles, J. A., Yeung, L. Y., Chin, E. J., & Lee, C. A. (2022). Rheology of Metasedimentary Rocks at the Base of the Subduction Seismogenic Zone. *Geochemistry, Geophysics, Geosystems*, 23(2), e2021GC010194. <https://doi.org/10.1029/2021GC010194>

Davis, P. B., & Whitney, D. L. (2008). Petrogenesis and structural petrology of high-pressure metabasalt pods, Sivrihisar, Turkey. *Contributions to Mineralogy and Petrology*, 156(2), 217–241. <https://doi.org/10.1007/s00410-008-0282-4>

Davoudian, A. R., Genser, J., Dachs, E., & Shabanian, N. (2008). Petrology of eclogites from north of Shahrekord, Sanandaj-Sirjan Zone, Iran. *Mineralogy and Petrology*, 92(3), 393–413. <https://doi.org/10.1007/s00710-007-0204-6>

Dekker, T. J. (1969). Finding a zero by means of successive linear interpolation. In B. Dejon & P. Henrici (Eds.), *Constructive aspects of the fundamental theorem of algebra: Proceedings of a Symposium, Zürich-Rüschlikon, Switzerland, 5.-7.6.1967*. Wiley-Interscience.

El-Shazly, A. K., Worthing, M. A., & Liou, J. G. (1997). Interlayered Eclogites, Blueschists and Epidote Amphibolites from NE Oman: A Record of Protolith Compositional Control and Limited Fluid Infiltration. *Journal of Petrology*, 38(11), 1461–1487. <https://doi.org/10.1093/petroj/38.11.1461>

- Escuder-Viruete, J., & Baumgartner, P. O. (2014). Structural evolution and deformation kinematics of a subduction-related serpentinite-matrix mélange, Santa Elena peninsula, northwest Costa Rica. *Journal of Structural Geology*, 66, 356–381. <https://doi.org/10.1016/j.jsg.2014.06.003>
- Federico, L., Crispini, L., Scambelluri, M., & Capponi, G. (2007). Ophiolite mélange zone records exhumation in a fossil subduction channel. *Geology*, 35(6), 499. <https://doi.org/10.1130/G23190A.1>
- Flores, K. E., Skora, S., Martin, C., Harlow, G. E., Rodríguez, D., & Baumgartner, P. O. (2015). Metamorphic history of riebeckite- and aegirine-augite-bearing high-pressure–low-temperature blocks within the Siuna Serpentinite Mélange, northeastern Nicaragua. *International Geology Review*, 57(5–8), 943–977. <https://doi.org/10.1080/00206814.2015.1027747>
- Geologische Bundesanstalt Österreich. (2021). *Geodaten—Blatt 152 Matrei in Osttirol (1:50.000)* (p. 4 datasets) [Map]. Tethys RDR. <https://doi.tethys.at/10.24341/tethys.65>
- Ghent, E., & Erdmer, P. (2011). 14—Very High-Pressure Epidote Eclogite from Ross River Area, Yukon, Canada, Records Deep Subduction. In L. F. Dobrzhinetskaya, S. W. Faryad, S. Wallis, & S. Cuthbert (Eds.), *Ultrahigh-Pressure Metamorphism* (pp. 441–457). Elsevier. <https://doi.org/10.1016/B978-0-12-385144-4.00013-8>
- Ghignone, S., Balestro, G., Gattiglio, M., & Borghi, A. (2020). Structural evolution along the Susa Shear Zone: The role of a first-order shear zone in the exhumation of meta-ophiolite units (Western Alps). *Swiss Journal of Geosciences*, 113(1), 17. <https://doi.org/10.1186/s00015-020-00370-6>
- Ghignone, S., Gattiglio, M., Balestro, G., & Borghi, A. (2020). *Geological Map of the Susa Shear Zone (Susa Valley, Western Alps)*.
- Ghignone, S., Sudo, M., Balestro, G., Borghi, A., Gattiglio, M., Ferrero, S., & Van Schijndel, V. (2021). Timing of exhumation of meta-ophiolite units in the Western Alps: New tectonic implications from ⁴⁰Ar/³⁹Ar white mica ages from Piedmont Zone (Susa Valley). *Lithos*, 404–405, 106443. <https://doi.org/10.1016/j.lithos.2021.106443>

- Hilalret, N., Reynard, B., Wang, Y., Daniel, I., Merkel, S., Nishiyama, N., & Petitgirard, S. (2007). High-Pressure Creep of Serpentine, Interseismic Deformation, and Initiation of Subduction. *Science*, 318(5858), 1910–1913. <https://doi.org/10.1126/science.1148494>
- Hirth, G., & Kohlstedt, D. (2003). Rheology of the upper mantle and the mantle wedge: A view from the experimentalists. In J. Eiler (Ed.), *Geophysical Monograph Series* (Vol. 138, pp. 83–105). American Geophysical Union. <https://doi.org/10.1029/138GM06>
- Hoover, W. F., Condit, C. B., Lindquist, P. C., Moser, A. C., & Guevara, V. E. (2022). Episodic Slow Slip Hosted by Talc-Bearing Metasomatic Rocks: High Strain Rates and Stress Amplification in a Chemically Reacting Shear Zone. *Geophysical Research Letters*, 49(21). <https://doi.org/10.1029/2022GL101083>
- Kaneko, Y., Maruyama, S., Terabayashi, M., Yamamoto, H., Ishikawa, M., Anma, R., Parkinson, C. D., Ota, T., Nakajima, Y., Katayama, I., Yamamoto, J., & Yamauchi, K. (2000). Geology of the Kokchetav UHP-HP metamorphic belt, Northern Kazakhstan. *The Island Arc*, 9(3), 264–283. <https://doi.org/10.1046/j.1440-1738.2000.00278.x>
- Keiter, M., Ballhaus, C., & Tomaschek, F. (2011). A new geological map of the Island of Syros (Aegean Sea, Greece): Implications for lithostratigraphy and structural history of the Cycladic Blueschist Unit. In M. Keiter, C. Ballhaus, & F. Tomaschek, *A new geological map of the Island of Syros (Aegean Sea, Greece): Implications for lithostratigraphy and structural history of the Cycladic Blueschist Unit*. Geological Society of America. <https://doi.org/10.1130/2011.2481>
- Kurz, W., Handler, R., & Bertoldi, C. (2008). Tracing the exhumation of the Eclogite Zone (Tauern Window, Eastern Alps) by $^{40}\text{Ar}/^{39}\text{Ar}$ dating of white mica in eclogites. *Swiss Journal of Geosciences*, 101(S1), 191–206. <https://doi.org/10.1007/s00015-008-1281-1>
- Liou, J. G., Zhang, R., & Ernst, W. G. (1998). *Mineral parageneses in the Piampaludo eclogitic body, Gruppo di Voltri, Western Ligurian Alps* [Text/html,application/pdf,text/html]. <https://doi.org/10.5169/SEALS-59291>

- Locatelli, M., Verlaquet, A., Agard, P., Federico, L., & Angiboust, S. (2018). Intermediate-depth brecciation along the subduction plate interface (Monviso eclogite, W. Alps). *Lithos*, 320–321, 378–402. <https://doi.org/10.1016/j.lithos.2018.09.028>
- Merdith, A. S., Williams, S. E., Collins, A. S., Tetley, M. G., Mulder, J. A., Blades, M. L., Young, A., Armistead, S. E., Cannon, J., Zahirovic, S., & Müller, R. D. (2021). Extending full-plate tectonic models into deep time: Linking the Neoproterozoic and the Phanerozoic. *Earth-Science Reviews*, 214, 103477. <https://doi.org/10.1016/j.earscirev.2020.103477>
- Okay, A. İ., & Satir, M. (2000). *Upper Cretaceous Eclogite-Facies Metamorphic Rocks from the Biga Peninsula, Northwest Turkey*.
- Ota, T., Terabayashi, M., & Katayama, I. (2004). Thermobaric structure and metamorphic evolution of the Iratsu eclogite body in the Sanbagawa belt, central Shikoku, Japan. *Lithos*, 73(1), 95–126. <https://doi.org/10.1016/j.lithos.2004.01.001>
- Petrie, M. B., Gilotti, J. A., McClelland, W. C., Van Staal, C., & Isard, S. J. (2015). Geologic Setting of Eclogite-facies Assemblages in the St. Cyr Klippe, Yukon–Tanana Terrane, Yukon, Canada. *Geoscience Canada*, 42(3), 327. <https://doi.org/10.12789/geocanj.2015.42.073>
- Philippon, M., Brun, J.-P., & Gueydan, F. (2012). Deciphering subduction from exhumation in the segmented Cycladic Blueschist Unit (Central Aegean, Greece). *Tectonophysics*, 524–525, 116–134. <https://doi.org/10.1016/j.tecto.2011.12.025>
- Pitzer, K. S., & Sterner, S. M. (1994). Equations of state valid continuously from zero to extreme pressures for H₂O and CO₂. *The Journal of Chemical Physics*, 101(4), 3111–3116. <https://doi.org/10.1063/1.467624>
- Ruh, J., Behr, W., & Tökle, L. (2024). Effect of Grain-Size and Textural Weakening in Polyphase Crustal and Mantle Lithospheric Shear Zones. *Tektonika*, 2(1). <https://doi.org/10.55575/tektonika3024.2.1.68>

- Rybacki, E., Konrad, K., Renner, J., Wachmann, M., Stöckhert, B., & Rummel, F. (2003). Experimental deformation of synthetic aragonite marble. *Journal of Geophysical Research: Solid Earth*, 108(B3). <https://doi.org/10.1029/2001JB000694>
- Schmidt, W. L., & Platt, J. P. (2022). Stress, microstructure, and deformation mechanisms during subduction underplating at the depth of tremor and slow slip, Franciscan Complex, northern California. *Journal of Structural Geology*, 154, 104469. <https://doi.org/10.1016/j.jsg.2021.104469>
- Şengün, F., Davis, P. B., Tunç, İ. O., & Yiğitbaş, E. (2012). Petrology and geochemistry of eclogites from the Biga Peninsula, Northwest Turkey. *Geodinamica Acta*, 25(3–4), 248–266. <https://doi.org/10.1080/09853111.2013.858954>
- Şengün, F., Yiğitbaş, E., & Tunç, İ. O. (2011). Geology and Tectonic Emplacement of Eclogite and Blueschists, Biga Peninsula, Northwest Turkey. *Turkish Journal of Earth Sciences*. <https://doi.org/10.3906/yer-0912-75>
- Shchipansky, A. A., Khodorevskaya, L. I., Konilov, A. N., & Slabunov, A. I. (2012). Eclogites from the Belomorian Mobile Belt (*Kola Peninsula*): Geology and petrology. *Russian Geology and Geophysics*, 53(1), 1–21. <https://doi.org/10.1016/j.rgg.2011.12.001>
- Sobolev, N. V., Dobretsov, N. L., Bakirov, A. B., & Shatsky, V. S. (1986). Eclogites from various types of metamorphic complexes in the USSR and the problems of their origin. In *Geological Society of America Memoirs* (Vol. 164, pp. 349–364). Geological Society of America. <https://doi.org/10.1130/MEM164-p349>
- Song, S., Niu, Y., Su, L., Zhang, C., & Zhang, L. (2014). Continental orogenesis from ocean subduction, continent collision/subduction, to orogen collapse, and orogen recycling: The example of the North Qaidam UHPM belt, NW China. *Earth-Science Reviews*, 129, 59–84. <https://doi.org/10.1016/j.earscirev.2013.11.010>
- Spear, F. S., Wolfe, O. M., Thomas, J. B., Hubbard, J. E., Castro, A. E., & Cheney, J. T. (2024). P–T Evolution of the Cyclades Blueschist Unit: Constraints on the Evolution of a Nascent Subduction

System From Zr-In-Rutile (ZiR) and Quartz-In-Garnet (QuiG) Thermobarometry. *Geochemistry, Geophysics, Geosystems*, 25(4), e2023GC011121. <https://doi.org/10.1029/2023GC011121>

Sterner, S. M., & Pitzer, K. S. (1994). An equation of state for carbon dioxide valid from zero to extreme pressures. *Contributions to Mineralogy and Petrology*, 117(4), 362–374. <https://doi.org/10.1007/BF00307271>

Stünitz, H., Neufeld, K., Heilbronner, R., Finstad, A. K., Konopásek, J., & Mackenzie, J. R. (2020). Transformation weakening: Diffusion creep in eclogites as a result of interaction of mineral reactions and deformation. *Journal of Structural Geology*, 139, 104129. <https://doi.org/10.1016/j.jsg.2020.104129>

Tagiri, M., Yano, T., Bakirov, A., Nakajima, T., & Uchiumi, S. (1995). Mineral parageneses and metamorphic P-T paths of ultrahigh-pressure eclogites from Kyrgyzstan Tien-Shan. *The Island Arc*, 4(4), 280–292. <https://doi.org/10.1111/j.1440-1738.1995.tb00150.x>

Tagiri, M., Takiguchi, S., Ishida, C., Noguchi, T., Kimura, M., Bakirov, A., Sakiev, K., Takahashi, M., Takasu, A., Bakirov, A., Togonbaeva, A., & Suzuki, A. (2010). Intrusion of UHP metamorphic rocks into the upper crust of Kyrgyzian Tien-Shan: P-T path and metamorphic age of the Makbal Complex. *Journal of Mineralogical and Petrological Sciences*, 105(5), 233–250. <https://doi.org/10.2465/jmps.071025>

Takasu, A. (1984). Prograde and Retrograde Eclogites in the Sambagawa Metamorphic Belt, Besshi District, Japan. *Journal of Petrology*, 25(3), 619–643. <https://doi.org/10.1093/petrology/25.3.619>

Tewksbury-Christle, C. M., Behr, W. M., Helper, M. A., & Stockli, D. F. (2023). *Tectonic Evolution of the Condrey Mountain Schist: An Intact Record of Late Jurassic to Early Cretaceous Franciscan Subduction and Underplating* [Preprint]. Preprints. <https://doi.org/10.22541/essoar.169603523.30791578/v1>

Togonbaeva, A., Takasu, A., Tagiri, M., Bakirov, A. B., Bakirov, A. A., & Sakiev, K. (2010). Newly described eclogites from the Neldy Formation, Makbal district, Northern Tien-Shan, Kyrgyzstan.

242 *Journal of Mineralogical and Petrological Sciences*, 105(2), 80–85.
 243 <https://doi.org/10.2465/jmps.091015c>

244 Tokle, L., Hirth, G., & Behr, W. M. (2019). Flow laws and fabric transitions in wet quartzite. *Earth and*
 245 *Planetary Science Letters*, 505, 152–161. <https://doi.org/10.1016/j.epsl.2018.10.017>

246 Tokle, L., Behr, W. M., Braden, Z., & Cisneros, M. (2022, December 14). *Structural Mapping of the*
 247 *Eclogite Zone, Tauern Window: Implications for the rheology of the subduction zone interface.*
 248 Fall Meeting 2022. <https://agu.confex.com/agu/fm22/meetingapp.cgi/Paper/1080102>

249 Tokle, L., Hufford, L. J., Behr, W. M., Morales, L. F. G., & Madonna, C. (2023). Diffusion Creep of
 250 Sodic Amphibole-Bearing Blueschist Limited by Microboudinage. *Journal of Geophysical*
 251 *Research: Solid Earth*, 128(9), e2023JB026848. <https://doi.org/10.1029/2023JB026848>

252 Tullis, T. E., Horowitz, F. G., & Tullis, J. (1991). Flow laws of polyphase aggregates from end-member
 253 flow laws. *Journal of Geophysical Research: Solid Earth*, 96(B5), 8081–8096.
 254 <https://doi.org/10.1029/90JB02491>

255 Wakabayashi, J. (2015). Anatomy of a subduction complex: Architecture of the Franciscan Complex,
 256 California, at multiple length and time scales. *International Geology Review*, 57(5–8), 669–746.
 257 <https://doi.org/10.1080/00206814.2014.998728>

258 Wassmann, S., & Stöckhert, B. (2013). Rheology of the plate interface—Dissolution precipitation creep
 259 in high pressure metamorphic rocks. *Tectonophysics*, 608, 1–29.
 260 <https://doi.org/10.1016/j.tecto.2013.09.030>

261 Whitney, D. L., Teyssier, C., Seaton, N. C. A., & Fornash, K. F. (2014). Petrofabrics of high-pressure
 262 rocks exhumed at the slab-mantle interface from the “point of no return” in a subduction zone
 263 (Sivrihisar, Turkey): Subduction petrofabrics. *Tectonics*, 33(12), 2315–2341.
 264 <https://doi.org/10.1002/2014TC003677>

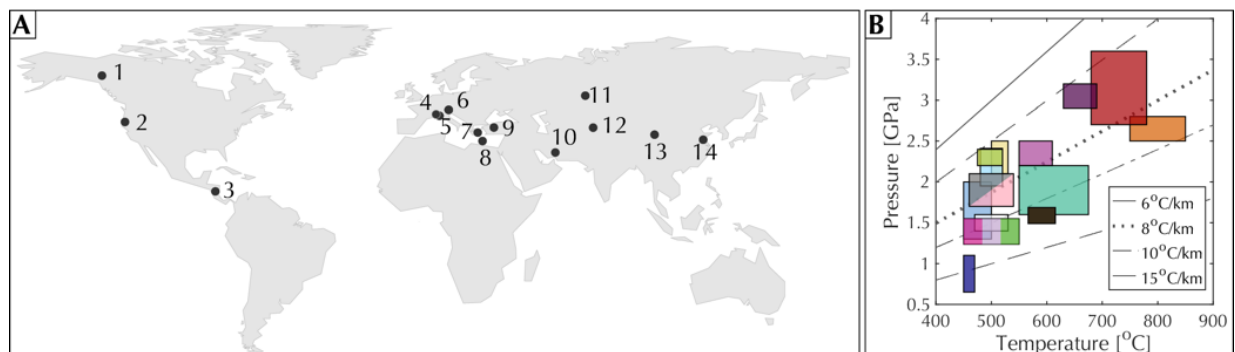
265 Withers, T. (2017, August 15). *The Pitzer and Sterner Equation of State for Water.*
 266 <https://github.com/forsterite/fugacity/>

267 Xu, Z., Zeng, L., Liu, F., Yang, J., Zhang, Z., McWilliams, M., & Liou, J. G. (2006). Polyphase
268 subduction and exhumation of the Sulu high-pressure–ultrahigh-pressure metamorphic terrane. In
269 B. R. Hacker, W. C. McClelland, & J. G. Liou, *Ultrahigh-pressure metamorphism: Deep*
270 *continental subduction*. Geological Society of America. [https://doi.org/10.1130/2006.2403\(05\)](https://doi.org/10.1130/2006.2403(05))
271 Zhang, Z. M., Liou, J. G., Zhao, X. D., & Shi, C. (2006). Petrogenesis of Maobei rutile eclogites from the
272 southern Sulu ultrahigh-pressure metamorphic belt, eastern China. *Journal of Metamorphic*
273 *Geology*, 24(8), 727–741. <https://doi.org/10.1111/j.1525-1314.2006.00665.x>
274 Zhang, J., & Green, H. W. (2007). On the Deformation of UHP Eclogite: From Laboratory to Nature.
275 *International Geology Review*, 49(6), 487–503. <https://doi.org/10.2747/0020-6814.49.6.487>
276 Zhang, R. Y., Liou, J. G., Omori, S., Sobolev, N. V., Shatsky, V. S., Iizuka, Y., Lo, C.-H., & Ogasawara,
277 Y. (2012). Tale of the Kulet eclogite from the Kokchetav Massive, Kazakhstan: Initial tectonic
278 setting and transition from amphibolite to eclogite. *Journal of Metamorphic Geology*, 30(5), 537–
279 559. <https://doi.org/10.1111/j.1525-1314.2012.00980.x>
280

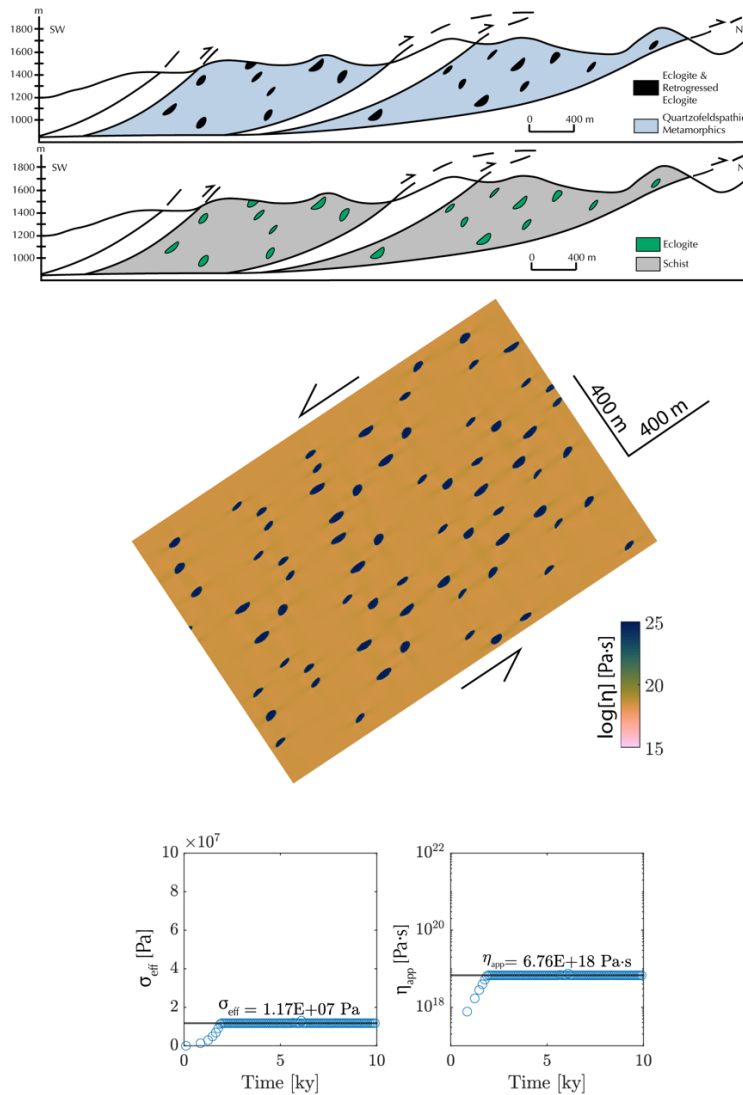
281 FIGURE CAPTIONS

282

283

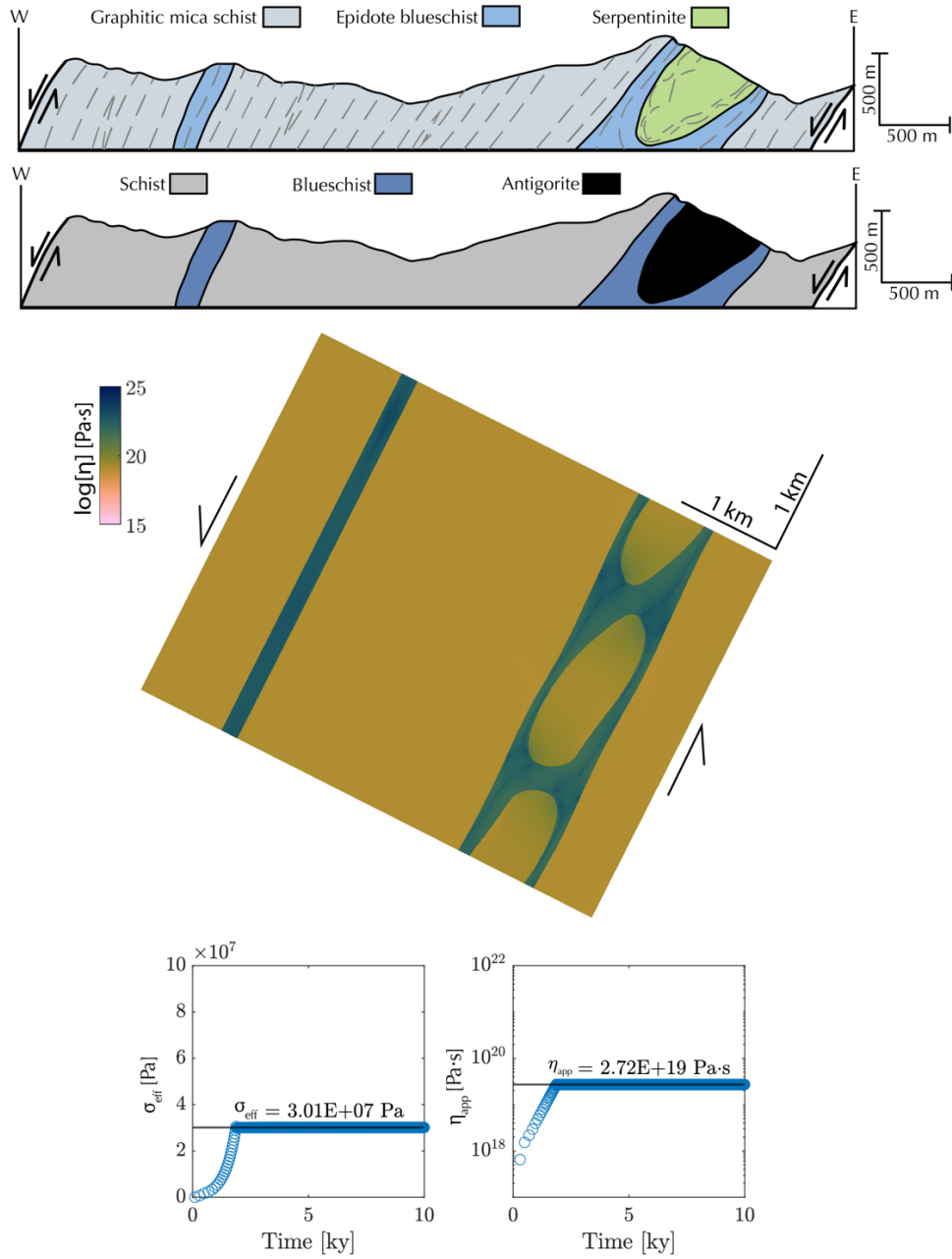


284 Figure S1. (A) Locations of the sections implemented. The numbers correspond to the sections as
 285 listed in Table S1 and Fig. 2. (B) Deformation conditions of the sections listed in Table S1. The
 286 colors correspond to the sections as shown in Fig. 2.



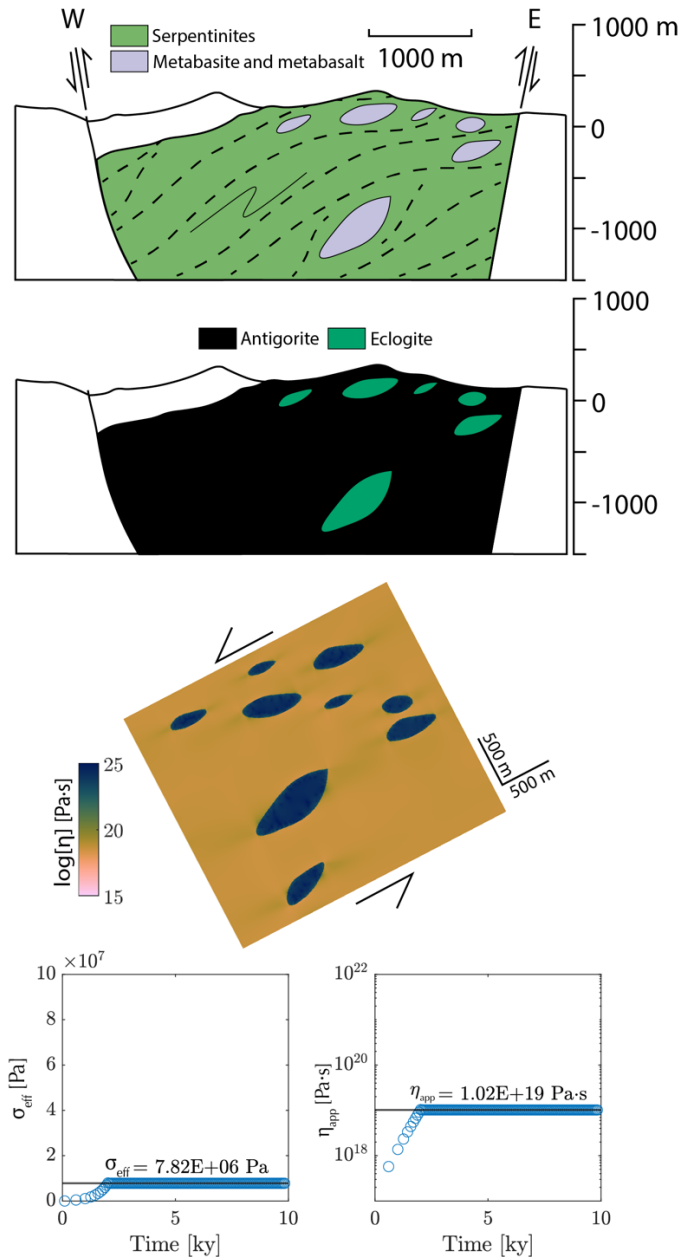
287

288 Figure S2.1. Yukon-Tanana Terrane, modified from Petrie et al. (2015). The section shows a later
 289 unit thrust into the shear zone. To obtain the thickness, this sliver was removed, and the total
 290 thickness remaining was considered the thickness of the section. The section was then extended
 291 into a rectangular input – preserving the geometry, spatial relations, and percentage distribution of
 292 blocks – and deformed. The viscosity distribution across the section at ~10 ky is shown. As an
 293 example of the final output, the effective strength and apparent viscosity evolution at 480°C is also
 294 provided.

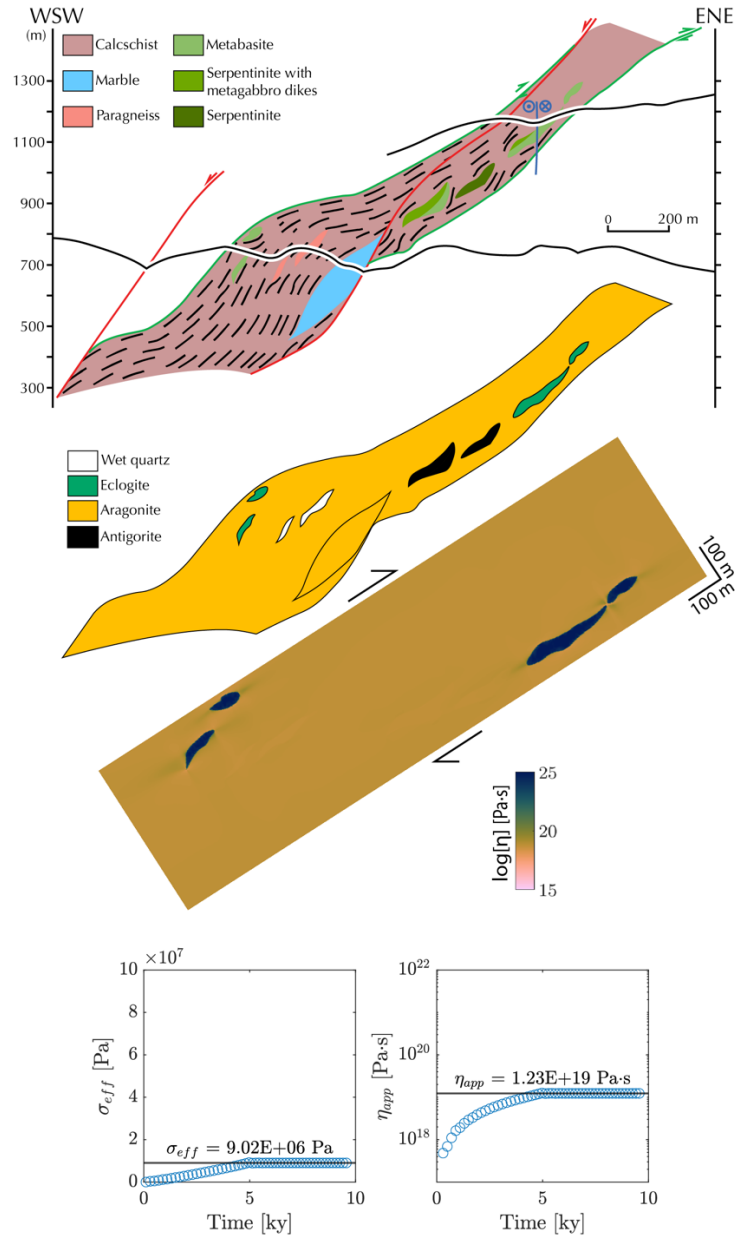


295

296 Figure S2.2. Condrey Mountain Schist, modified from Tewksbury-Christle et al. (2023). The
 297 section was extended into a rectangular input – preserving the geometry, spatial relations, and
 298 percentage distribution of blocks – and deformed. The viscosity distribution across the section at
 299 ~10 ky is shown. As an example of the final output, the effective strength and apparent viscosity
 300 evolution at 450°C is also provided.

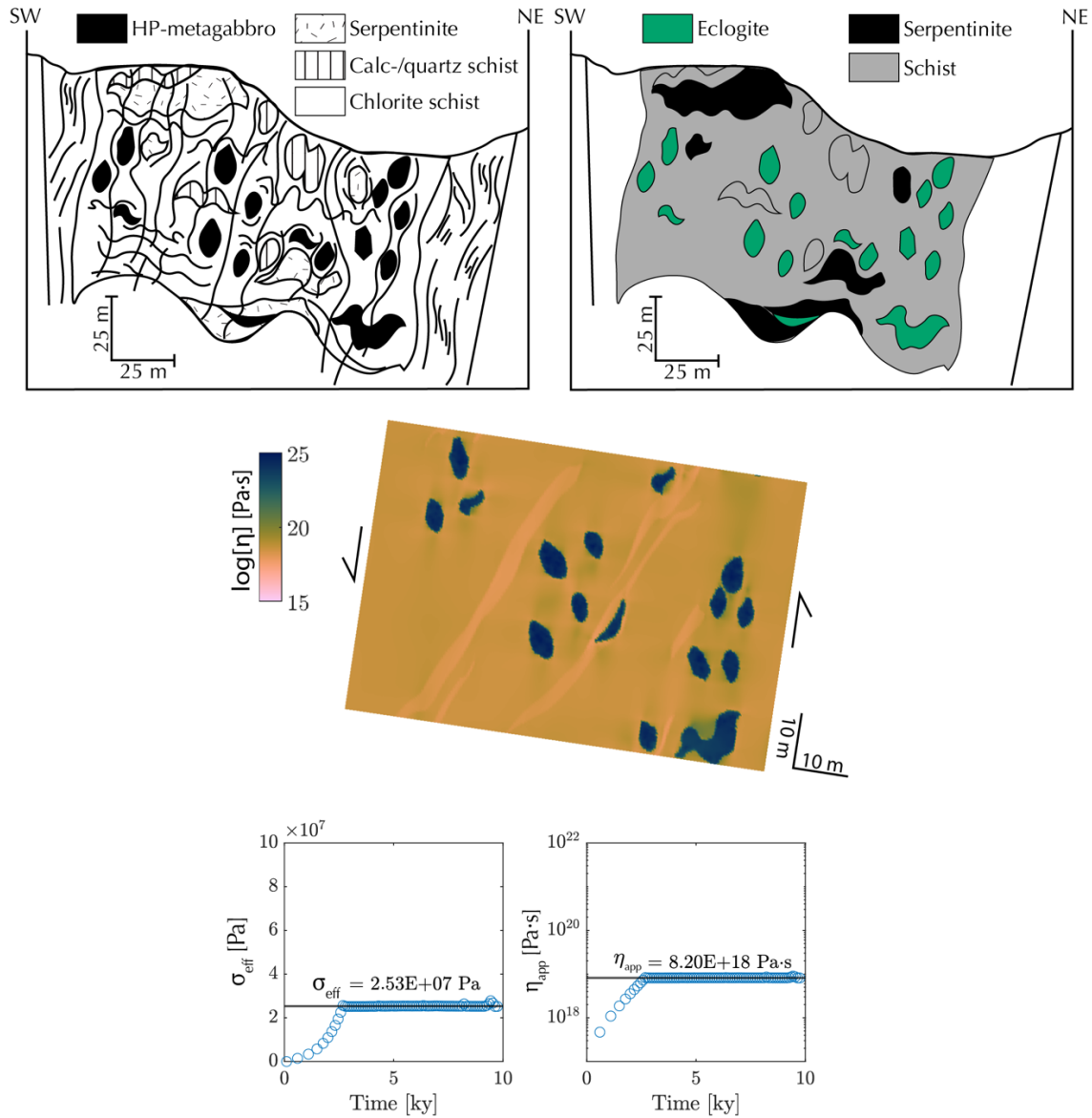


301
 302 Figure S2.3. Siuna Serpentinite Mélange, modified from Andjić et al. (2019). The underlying unit
 303 below the mélange is unreported, but the aforementioned reference gives an estimated thickness
 304 of 2.5 km. This estimate, with the provided section, was then extended into a rectangular input –
 305 preserving the geometry, spatial relations, and percentage distribution of blocks – and deformed.
 306 The viscosity distribution across the section at ~10 ky is shown. As an example of the final output,
 307 the effective strength and apparent viscosity evolution at 565°C is also provided.



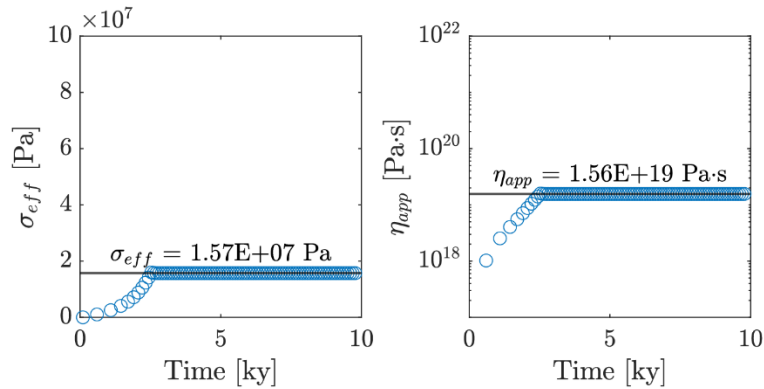
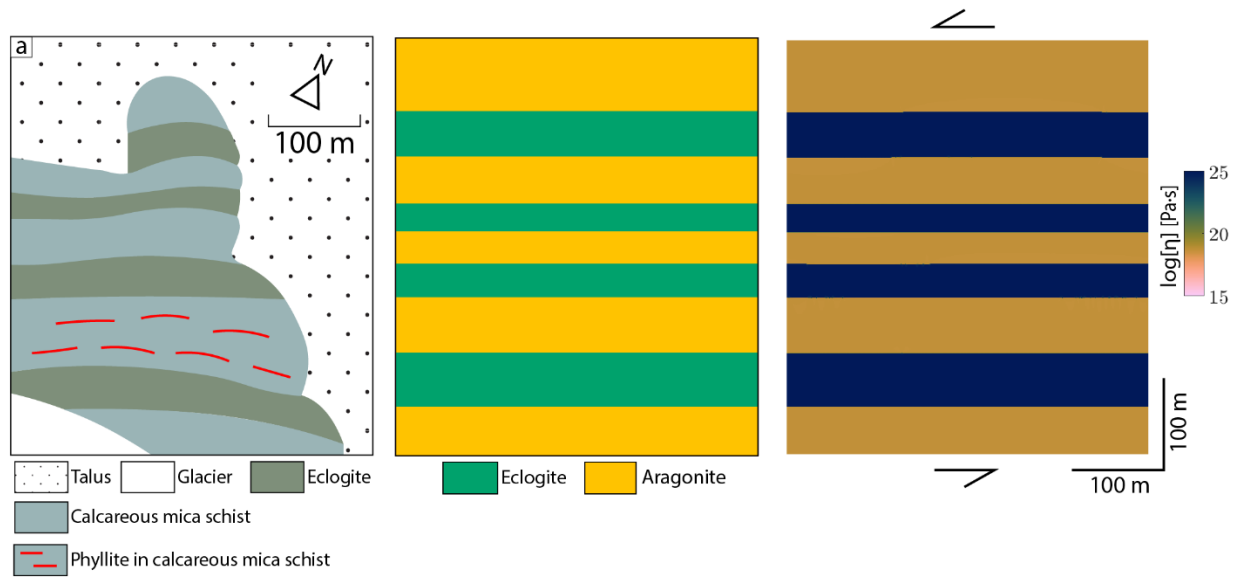
308

309 Figure S2.4. Susa Shear Zone, modified from Ghignone et al. (2020). The thickness of the section
 310 is taken from the lower portion, as these report less overprinting by later structures. The section
 311 was then extended into a rectangular input – preserving the geometry, spatial relations, and
 312 percentage distribution of blocks – and deformed. The viscosity distribution across the section at
 313 ~10 ky is shown. As an example of the final output, the effective strength and apparent viscosity
 314 evolution at 500°C is also provided.



315

316 Figure S2.5. Voltri Massif Mélange Zone, modified from Federico et al. (2007). The calcschists
 317 and quartz schist blocks were grouped together in the original map, thus were assigned a schist
 318 rheology. The matrix is also assigned a schist rheology, as it best represents the rheology of
 319 metasediments at high pressure conditions. The section was then extended into a rectangular input
 320 – preserving the geometry, spatial relations, and percentage distribution of blocks – and deformed.
 321 The viscosity distribution across the section at ~10 ky is shown. As an example of the final output,
 322 the effective strength and apparent viscosity evolution at 450°C is also provided.



323

324 Figure S2.6a. Tauern Eclogite Zone, modified from Geologische Bundesanstalt Österreich (2021).

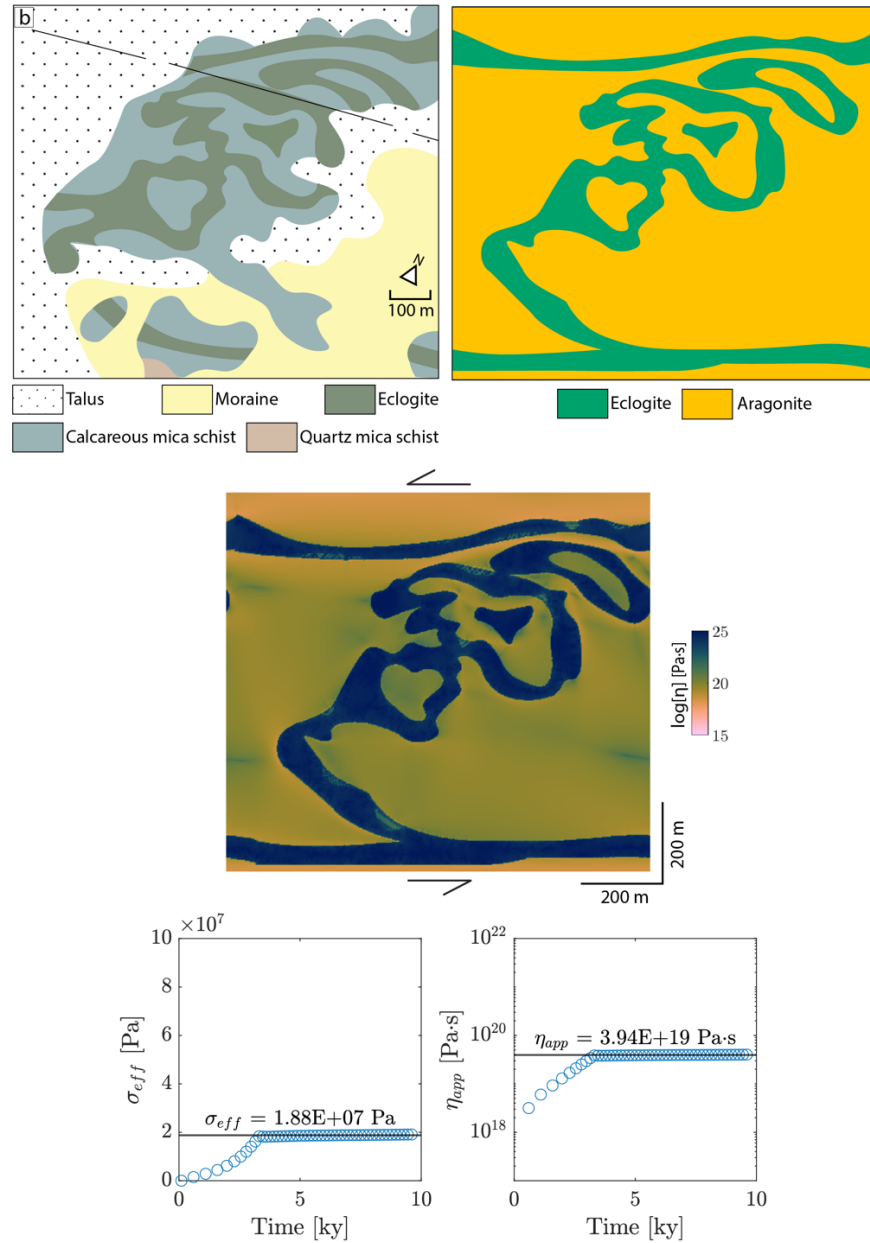
325 The map shows vertical beds and Quaternary cover over the unit. The units and structures were

326 projected based on field observations (Tokle et al., 2022) of nearby units to generate a rectangular

327 input, which was deformed. The viscosity distribution across the section at ~10 ky is shown. As

328 an example of the final output, the effective strength and apparent viscosity evolution at 460°C is

329 also provided.



330

331 Figure S2.6b. Tauern Eclogite Zone, modified from Geologische Bundesanstalt Österreich (2021).

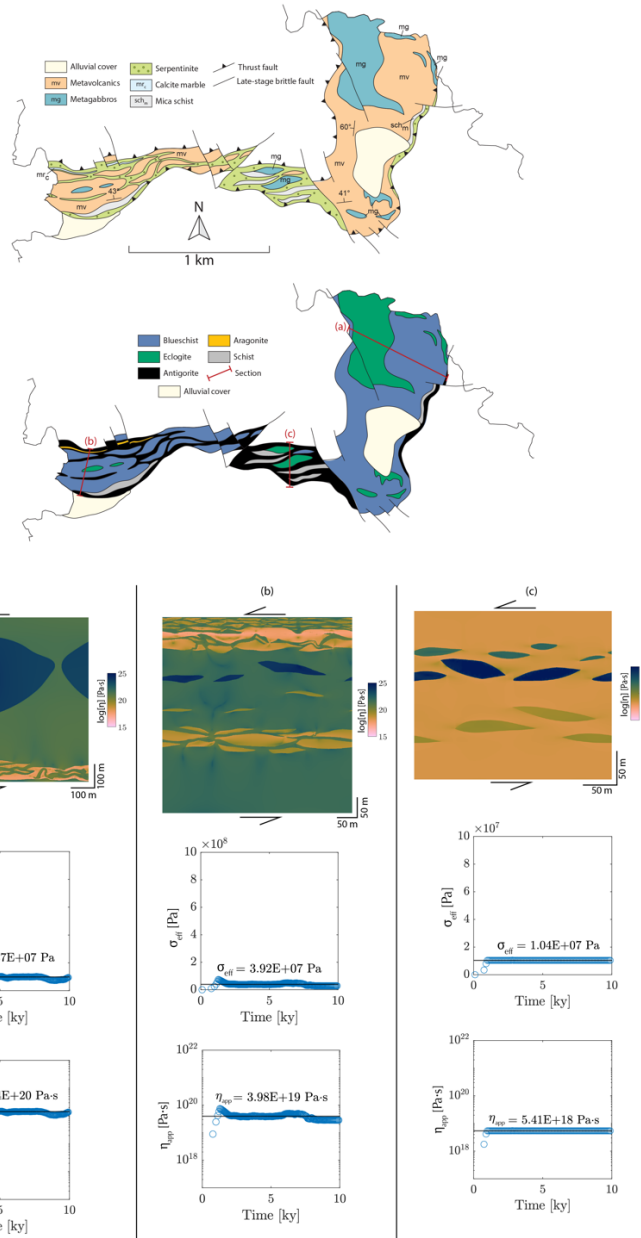
332 The map shows vertical beds and Quaternary cover over the unit. The units and structures were

333 projected based on field observations (Tokle et al., 2022) of nearby units to generate a rectangular

334 input, which was deformed. The viscosity distribution across the section at ~10 ky is shown. As

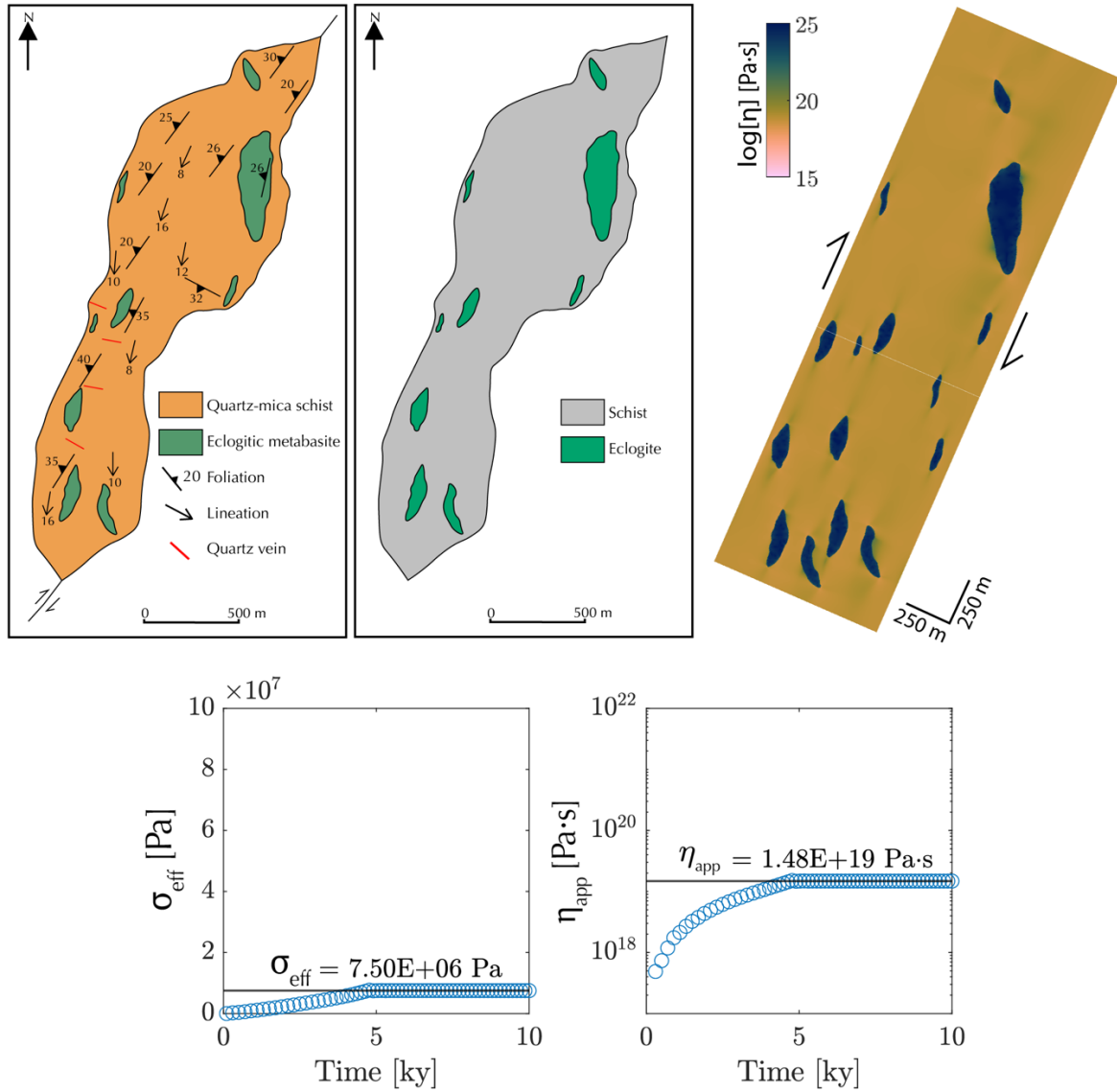
335 an example of the final output, the effective strength and apparent viscosity evolution at 460°C is

336 also provided.



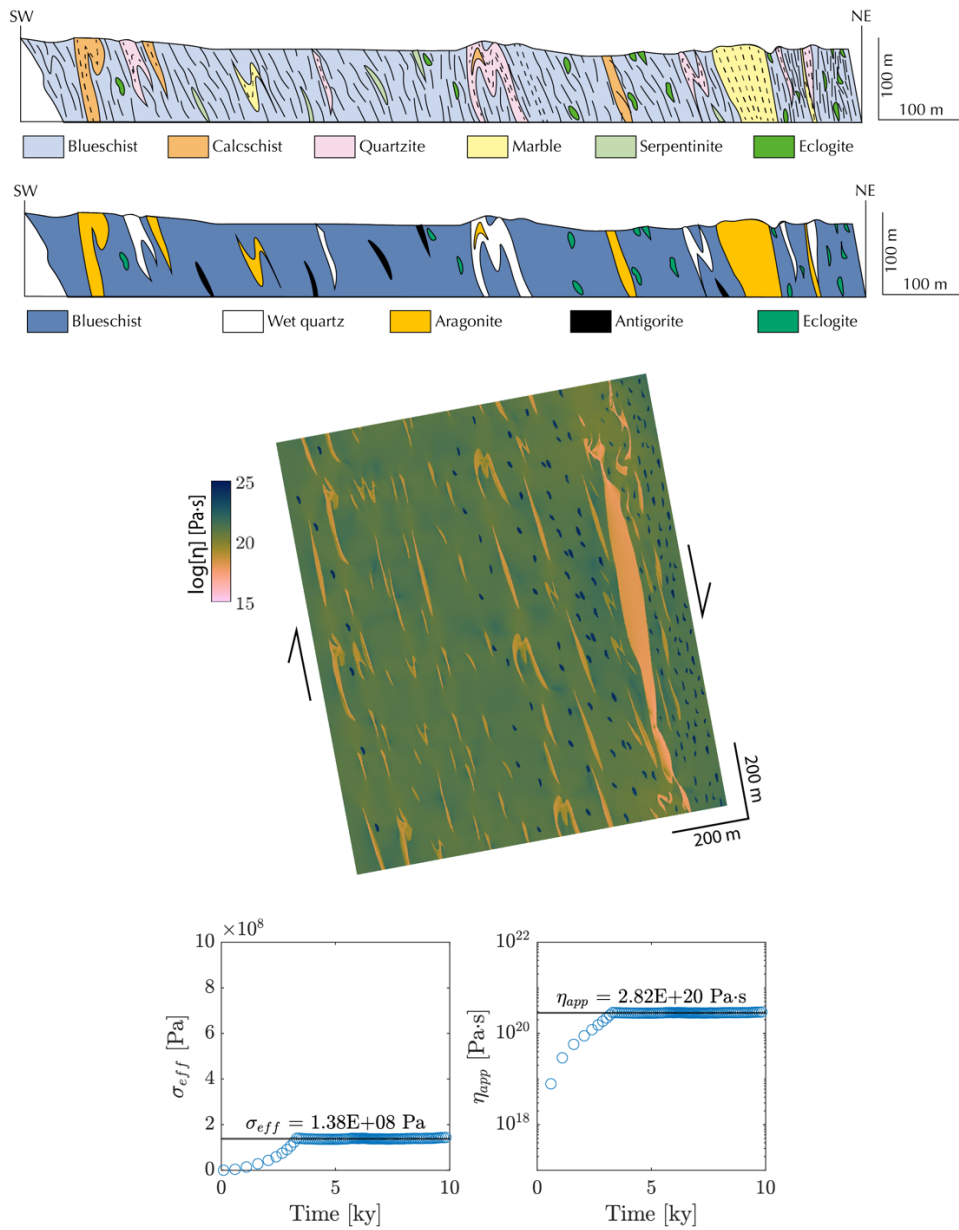
337

338 Figure S2.7a,b,c. Cycladic Blueschist unit, modified from Keiter et al. (2011). The map contains
 339 detailed structural measurements, which were used to generate cross sections, preserving the
 340 geometry, spatial relations, and percentage distribution of blocks. This section was then extended
 341 a rectangular input and deformed. The viscosity distribution across the section at ~10 ky is shown.
 342 As an example of the final output, the effective strength and apparent viscosity evolution at 475°C
 343 of each section is also provided.



344

345 Figure S2.8. Camlica HP Slice, modified from Şengün et al. (2011). The map shows a transposed
 346 deep interface shear zone, with high-angle foliations. Based on the structures and the literature, the
 347 thickness of the section was taken as the thickest portion of the shear zone. This was then extended
 348 to a rectangular input – preserving the geometry, spatial relations, and percentage distribution of
 349 blocks – and deformed. The viscosity distribution across the section at ~10 ky is shown. As an
 350 example of the final output, the effective strength and apparent viscosity evolution at 550°C is also
 351 provided.



352

353

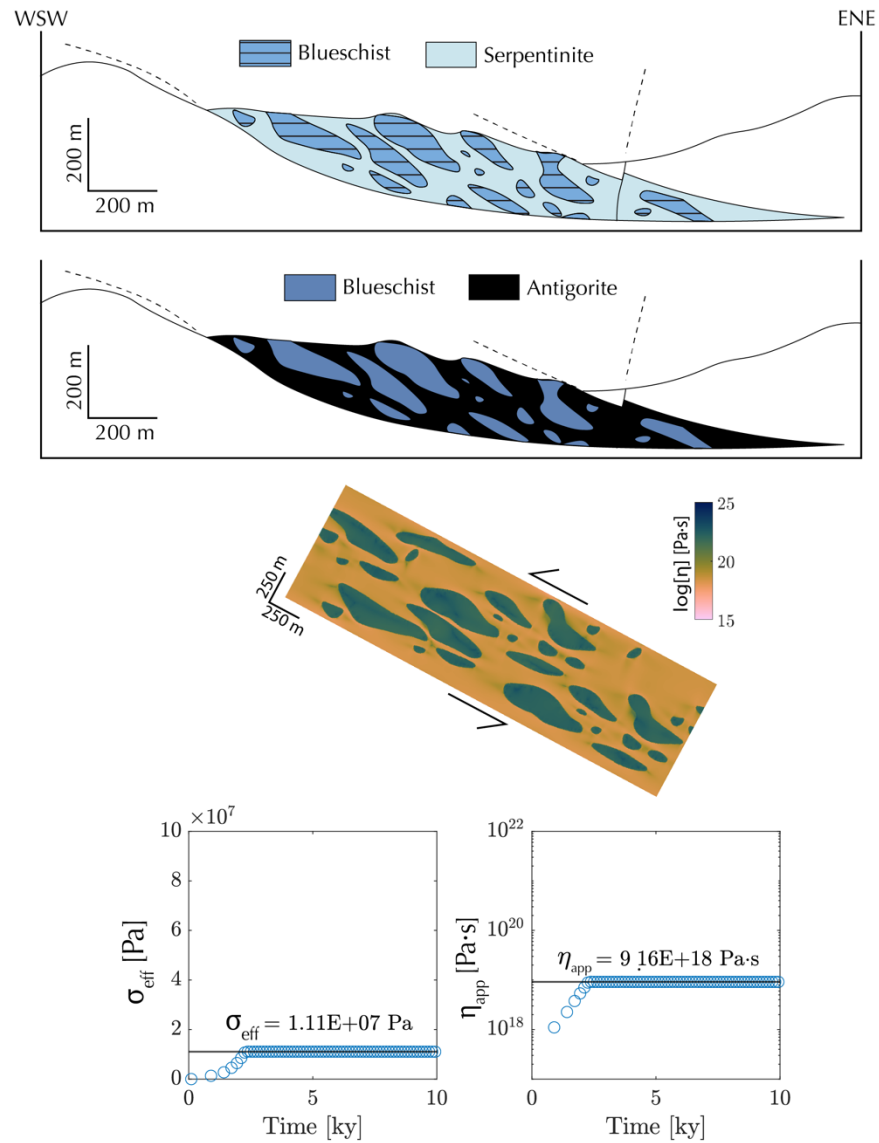
354

355

356

357

Figure S2.9. Halilbagi Unit, modified from Whitney et al. (2014). Using a large-scale section in the reference as a guide, the section provided was projected to a rectangular input, preserving the geometry, spatial relations, and percentage distribution of blocks. The rectangular input was then deformed, and the viscosity distribution across the section at ~ 10 ky is shown. As an example of the final output, the effective strength and apparent viscosity evolution at 475°C is also provided.



358

359

Figure S2.10. Seghin Complex, modified from Angiboust et al. (2016). The section was extended

360

into a rectangular input – preserving the geometry, spatial relations, and percentage distribution of

361

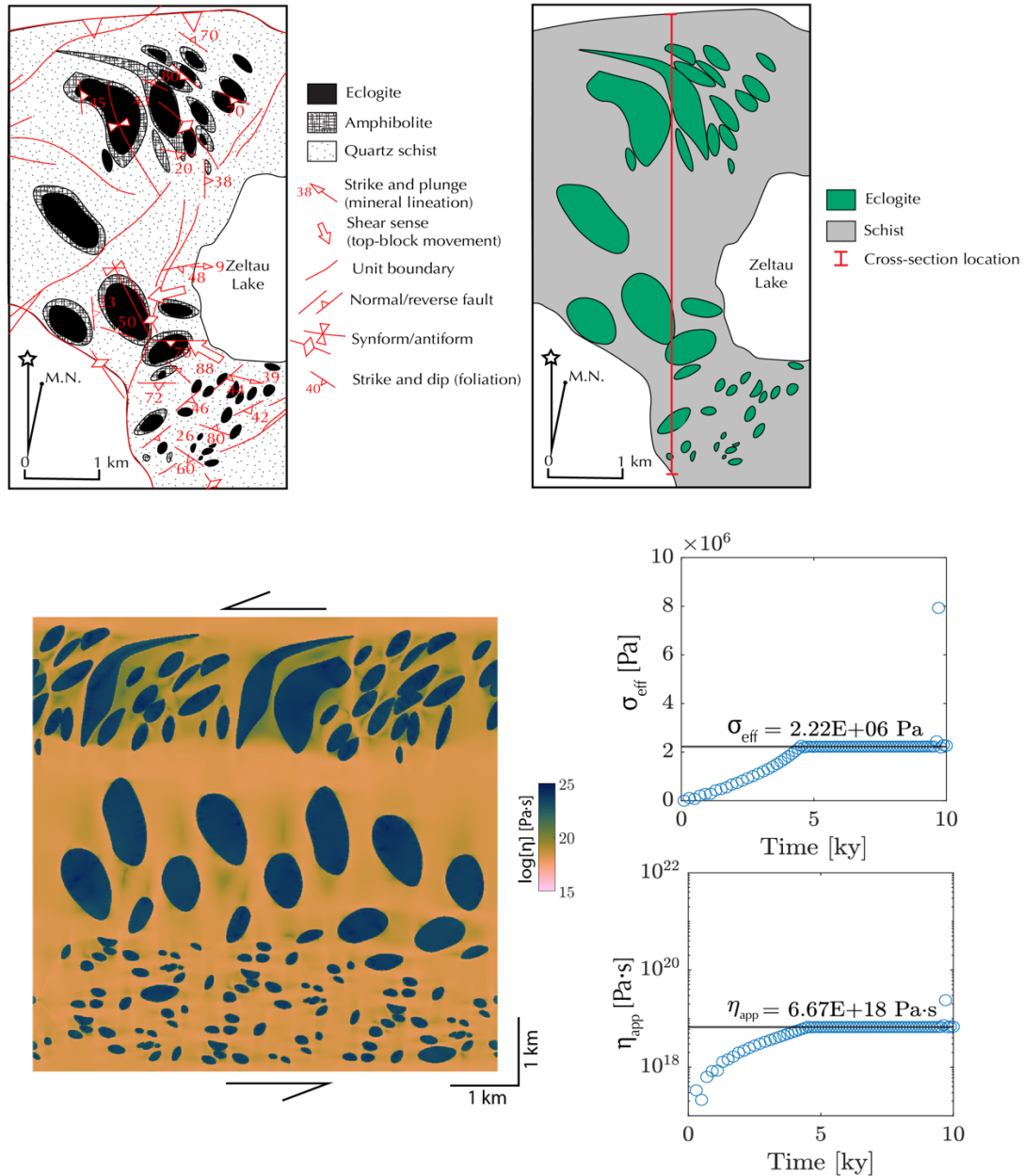
blocks – and deformed. The viscosity distribution across the section at ~10 ky is shown. As an

362

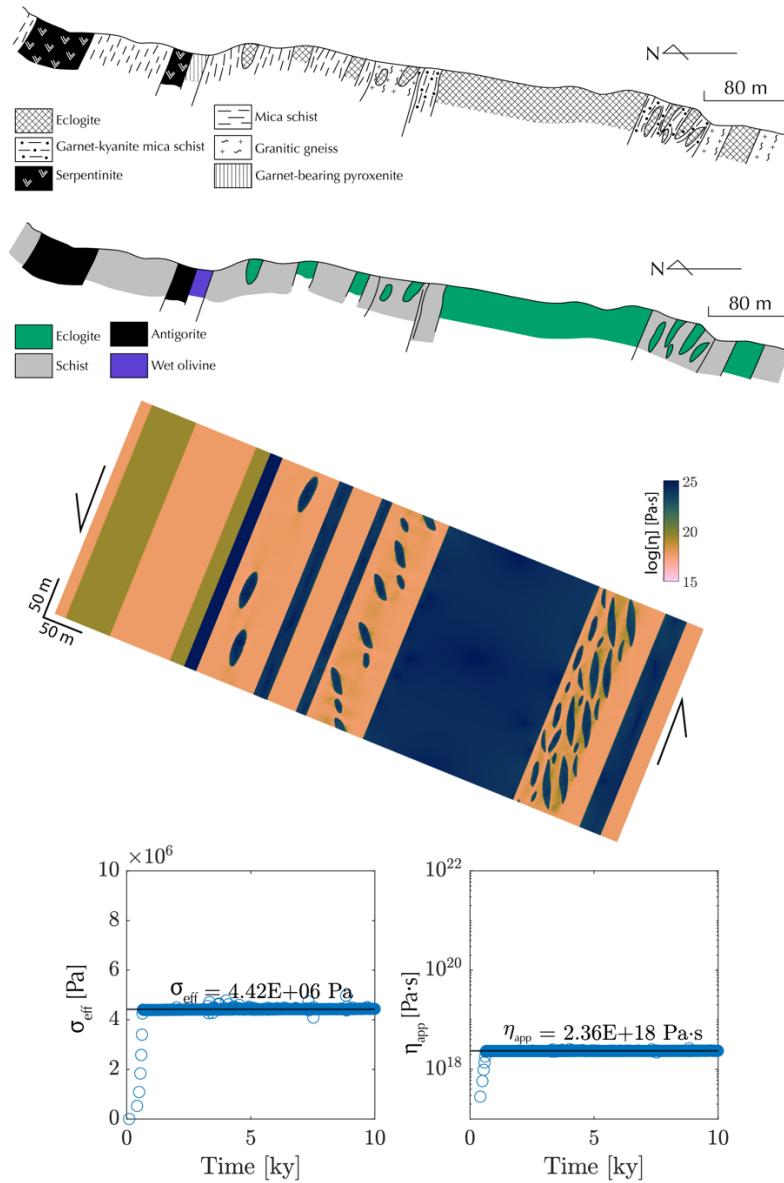
example of the final output, the effective strength and apparent viscosity evolution at 470°C is also

363

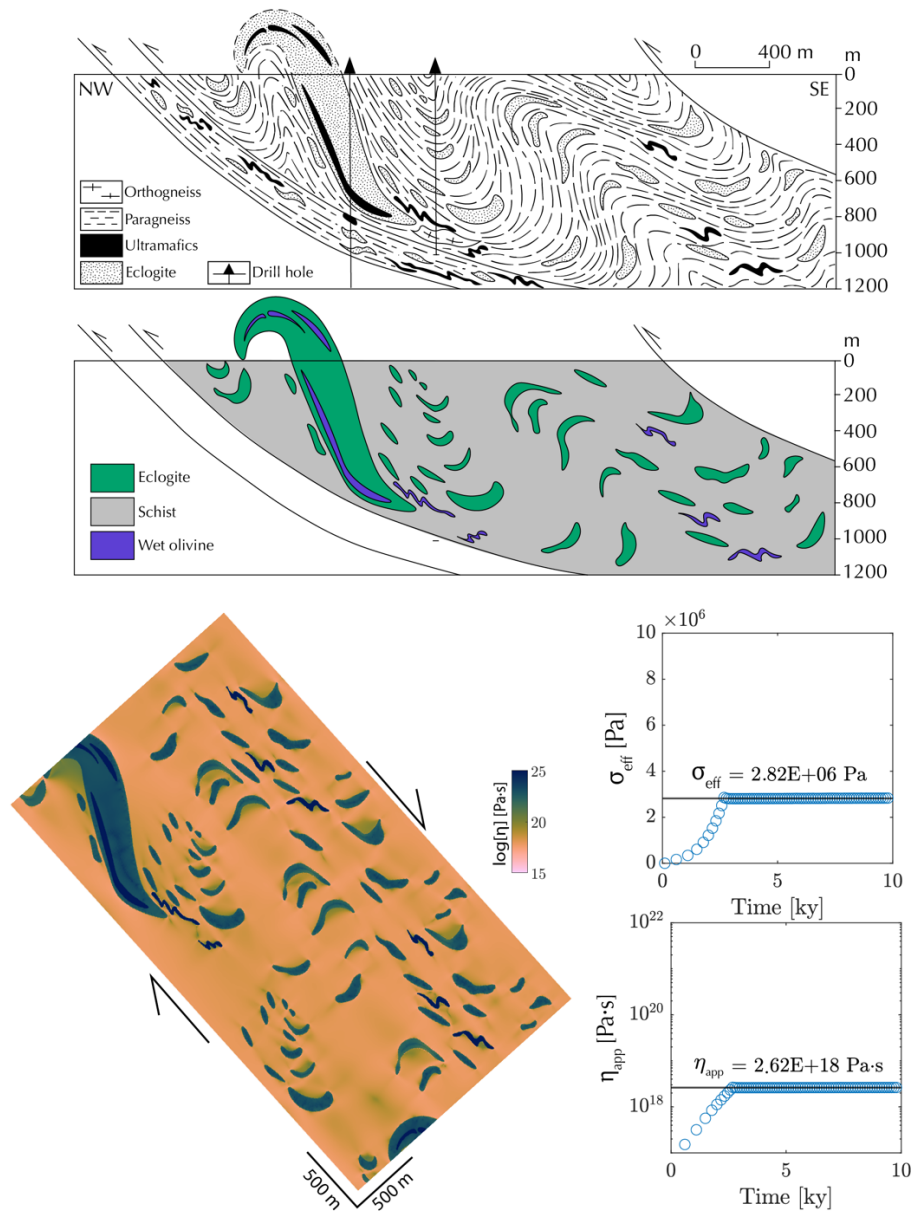
provided.



No Figure S2.12



371
 372 Figure S2.13. Dulan UHPM Terrane, modified from Song et al. (2014). The literature reports that
 373 the unit mapped is bounded at the top and bottom, though not explicitly shown in the figure. Thus,
 374 the thickness of the shear zone is taken as the thickness of the published section. From the section,
 375 a rectangular input – preserving the geometry, spatial relations, and percentage distribution of
 376 blocks – was generated. The rectangular input was then deformed, and the viscosity distribution
 377 across the section at ~10 ky is shown. As an example of the final output, the effective strength and
 378 apparent viscosity evolution at 630°C is also provided.



379

380 Figure S2.14. Maobei Slice, modified from Xu et al. (2006). The thickness of the section is taken
 381 based on the structural measurements on the surface. The section was then extended to a
 382 rectangular input – preserving the geometry, spatial relations, and percentage distribution of blocks
 383 – and deformed. The viscosity distribution across the section at ~10 ky is shown. As an example
 384 of the final output, the effective strength and apparent viscosity evolution at 750°C is also
 385 provided.

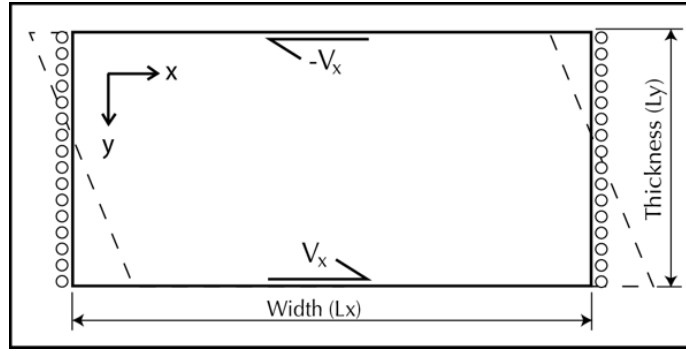


Figure S3. Set-up implemented to modelled sections, with no slip top and bottom boundaries, and periodic left and right boundaries. Sections are oriented for top to the left shearing, with shear velocity V_x (see Table A1).

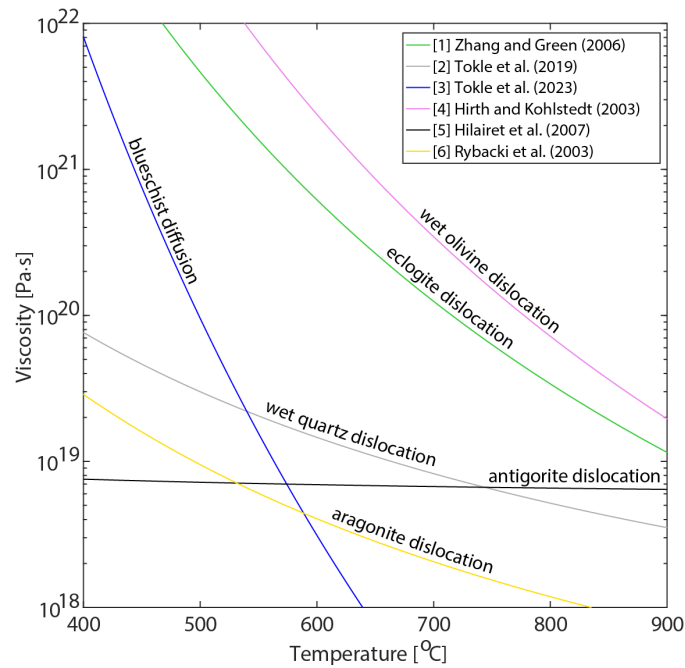


Figure S4. Implemented viscous rheologies at a strain rate of 1×10^{-12} 1/s. See Table A2 for parameters.

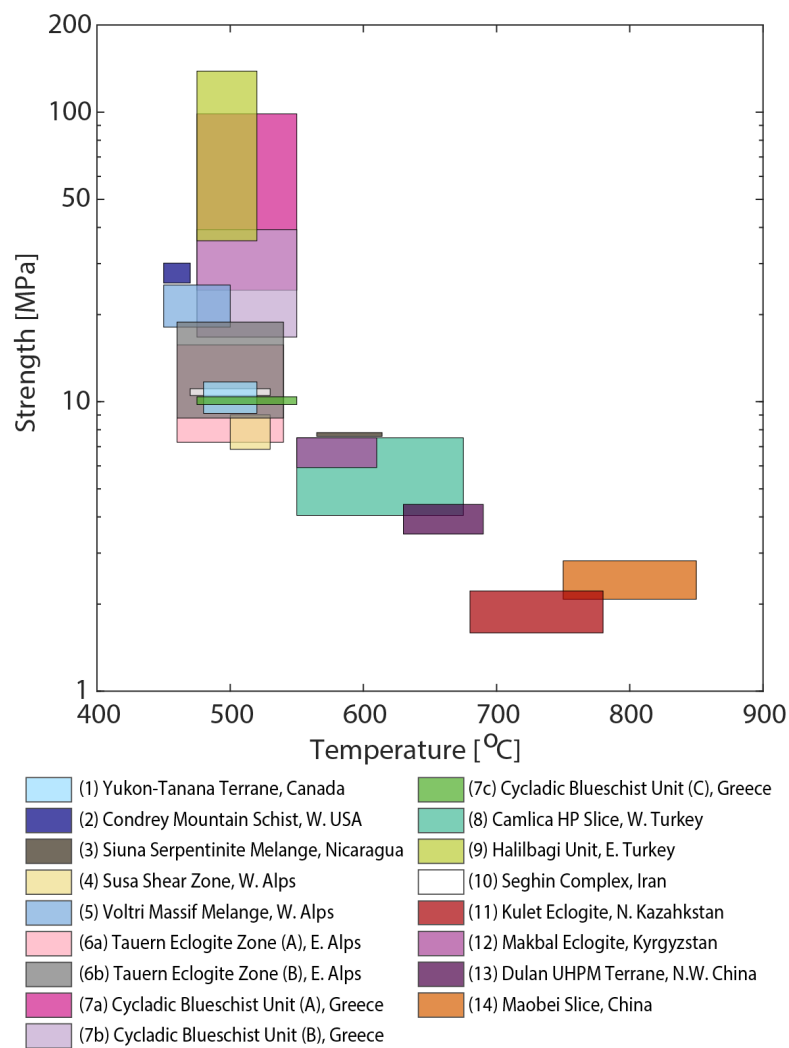
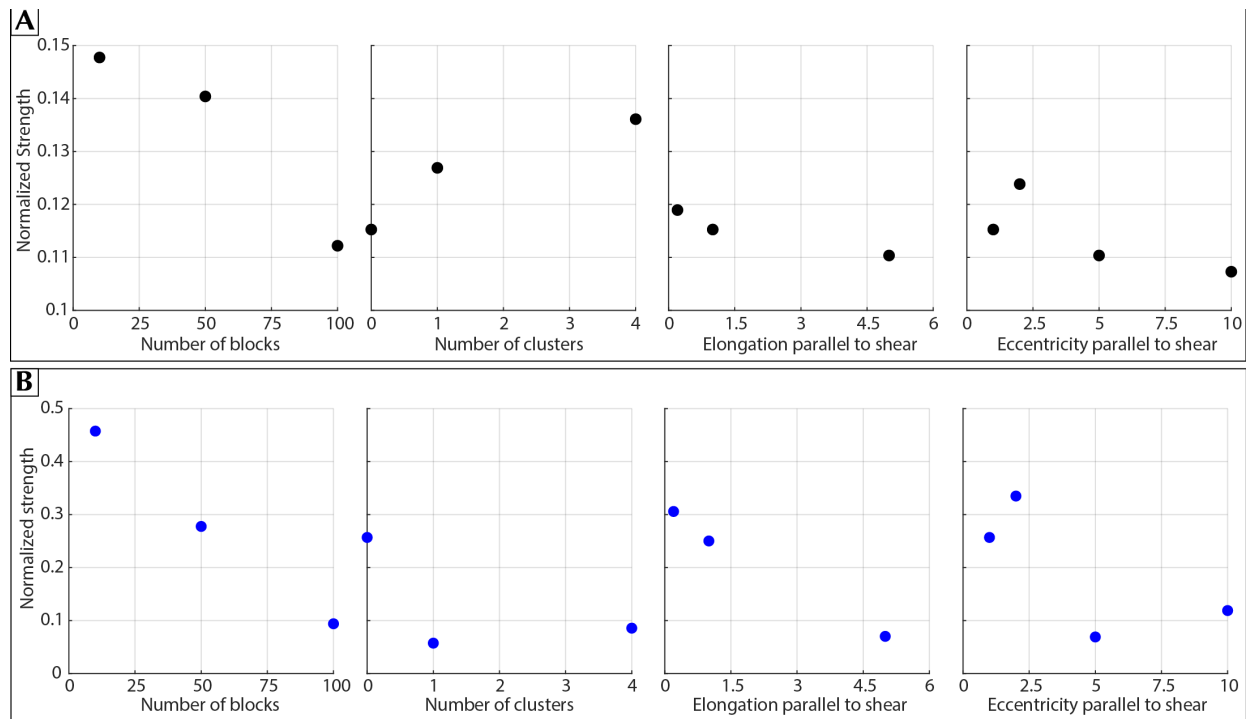


Figure S5. Strength distribution of the 17 modeled shear zones.



398

Figure S6. Effect of block geometry and distribution on model strength, with (A) weak matrix-strong block and (B) strong matrix-weak block combinations. The strength of these sections are normalized to strength from the mixing model of Tullis et al. (1991).

Unit	Locality	Dimensions ^a		Deformation Conditions		Age of Deformation	
		Ly (m)	Lx (m)	P (GPa)	T (°C)	Age (Ma)	V _x ^b (cm/yr)
1 Yukon-Tanana Terrane	Yukon, Canada	2735	4104	2.33	480	266	15.0
2 Condrey Mountain Schist	Klamath Mtns., W. USA	4741	3754	0.65 - 1.1	450 - 470	133 - 119	16.6
3 Siuna Serpentinite Melange	N.E. Nicaragua	2479	2838	1.5 - 1.7	565 - 614	~140	6.0
4 Susa Shear Zone	W. Alps	432	1608	2.1 - 2.5	500 - 530	44 - 37	1.0
5 Voltri Massif Mélange Zone	W. Alps	77	53	1.3 - 2.0	450 - 500	43 - 40	0.8
6a Tauern Eclogite Zone	E. Alps	441	385	1.9	460 - 540	38 - 32	1.4
6b		931	1011				
7a	Syros, Greece	691	868	1.1 - 1.8	475 - 550	~45	1.5
7b Cycladic Blueschist Unit		483	468				
7c		248	291				
8 Camlica HP Slice	Biga, W. Turkey	938	3205	1.2 - 2.2	550 - 675	69 - 65	1.5
9 Halilbagi Unit	Sivrihisar, E. Turkey	973	1136	2.2 - 2.4	475 - 520	88.5	1.5
10 Seghin Complex	Zagros, Iran	945	3119	1.4 - 1.6	470 - 530	72.7 - 62.5	3.6
11 Kulet Eclogite	Kokchetav Massif, N. Kazakhstan	6658	6808	2.7 - 3.6	680 - 780	530	7.0
12 Makbal Eclogite	Tien Shan, Kyrgyzstan	805	354	2.2 - 2.5	550 - 610	480	2.0
13 Dulan UHPM Terrane	North Qaidam Belt, N.W. China	727	276	2.9 - 3.2	630 - 690	438 - 420	4.3
14 Maobei Slice	Dabie-Sulu, China	1942	3515	2.5 - 2.8	750 - 850	221 - 216	6.6

^a See Figure S1 for orientation of sections. Resolution is dependent on the scale of the source image, and is set using a square pixel with dimensions ~1% of L_x. ^b Shear zone velocities are taken from plate reconstruction convergence velocities of Meredith et al. (2021).

TABLE S1. SOURCE MATERIAL FOR MODELED SHEAR ZONES

Map Source	Deformation Conditions Source	Age Source	Estimated Location of Unit		
			Latitude (°N)	Longitude (°E)	Plate A
Petrie et al. (2015)	Ghent & Erdmer (2011)	Petrie et al. (2015)	61.46	-132.66	16104
Tewksbury-Christle et al. (2023)	Tewksbury-Christle et al. (2023)	Tewksbury-Christle et al. (2023)	41.94	-123.02	101
Andjić et al. (2019)	Flores et al. (2015)	Flores et al. (2015)	13.60	-84.81	2035
Ghignone, Gattiglio, et al. (2020)	Ghignone, Balestro, et al. (2020)	Ghignone et al. (2021)	45.15	7.08	305
Federico et al. 2007	Liou et al., 1988	Federico et al. (2007)	44.54	8.48	305
Geologische Bundesanstalt Österreich (2021)	Tokle et al., (2022)	Kurz et al. (2008)	47.06	12.35	701
Keiter et al. (2011)	Spear et al. (2024)	Philippon et al. (2012)	37.49	24.91	301
Şengün et al. (2011)	Şengün et al. (2014)	Şengün et al. (2014)	33.93	26.49	521
Whitney et al. (2014)	Davis & Whitney (2006)	Okay & Satir (2000)	39.60	31.25	521
Angiboust et al. (2016)	Angiboust et al. (2016)	Angiboust et al. (2016)	29.10	56.95	301
Kaneko et al. (2000)	Zhang et al. (2012)	Zhang et al. (2012)	53.02	69.49	460
Sobolev et al. (1986), Tagiri et al. (2010)	Togonbaeva et al. (2010)	Tagiri et al. (1995)	39.55	72.75	590
Song et al. (2014)	Song et al. (2014)	Song et al. (2014)	36.60	98.44	451
Xu et al. (2006)	Xu et al. (2006)	Zhang et al. (2006)	34.47	118.77	601

Parameters for Shear Velocity (Merdith et al., 2021)

Plate B	Notes	Reference Latitude (°N)	Reference Longitude (°E)
16106	Yukon-Tanana / Cassier (NAM)	68.70	-123.45
902	Farallon/North America	41.94	-123.02
224	Chortis/Carribean (proto-CHIP?)	9.17	-44.55
307	Armorica/Adria	50.01	12.89
307	Armorica/Adria	44.52	8.50
301	Africa/Eurasia	47.06	12.35
			12.35
308	Eurasia/Diniride	34.50	21.87
522	Sakarya/Menderes-Taurides Block	43.67	35.24
522	Sakarya/Menderes-Taurides Block	39.68	31.24
503	Eurasia/Arabia	28.20	56.23
980441	Chu Yili/Big ocean plate	53.04	69.73
602	Northern Pamirs/South China	39.28	72.85
456	Alashan/Qaidam-Qilian	39.06	92.35
602	North China/South China	31.34	117.57

TABLE S2. RHEOLOGICAL INPUT PARAMETERS

Rheology	Reported Lithologies ^a	n	m	r	Q ^b [kJ/mol]	A [MPa ^{-n-r} um ^m s ⁻¹]	Reference ^c
1 Eclogite	Eclogite, metabasalt, metagabbro	3.5	0	0	403 + 27.2P	103.3	J. Zhang & Green, 2007 (disl.)
2 Wet Quartz	Quartzite, metachert	4	0	1 ^d	125	1.75×10^{-12}	Tokle et al., 2019 (disl.)
3 Blueschist	Blueschist	2	1 ^e	0	383	2.97×10^{-11}	Tokle et al., 2023 (diff.)
4 Wet Olivine	Meta-peridotite, peridotite	3.5	0	1.2 ^f	480 + 22P	90	Hirth & Kohlstedt, 2003 (disl.)
5 Schist	Quartz schist, mica schist	4	0	1 ^d	125	1.75×10^{-12}	Tokle et al., 2019 (disl.)
6 Antigorite	Serpentinite	3.6	0	0	8.9 + 3.2P	$e^{-0.86}$	Hilaret et al., 2007 (disl.)
7 Aragonite	Marble, calcschist	5.2	0	0	249	$e^{-0.6}$	Rybacki et al., 2003 (disl.)

Note: The parameters following the relation $\dot{\epsilon} = A\sigma^n \frac{f^r}{d^m} \exp\left(-\frac{Q}{RT}\right)$, where $\dot{\epsilon}$ is strain rate (1/s), σ is stress (MPa), f is fugacity (MPa), d is grain size (μm), Q is activation enthalpy (kJ/mol), R is the gas constant ($8.314 \frac{\text{J}}{\text{mol}\cdot\text{K}}$), T is temperature (K), and n , m , and r are the stress,

^a These are the lithologies as mapped, which were re-interpreted based on available flow laws.

^b Activation enthalpy is reported as either Q or as activation energy (E_a), volume (V), and pressure (P), as $Q = E_a + PV$.

^c disl. = dislocation creep flow laws, diff. = diffusion creep flow laws.

^d Quartz water fugacity is implemented using the analytical solution of (Sterner & Pitzer, 1994), given as $\ln f = \left[\ln q + \frac{A^{\text{res}}}{RT} + \frac{P}{qRT} \right]_{P,T} +$

$\ln(RT) - 1$, where f is fugacity, A^{res} is residual Helmholtz energy, and q is molar density. Molar volume and fugacity of pure water was determined using (Pitzer & Sterner, 1994), and the Dekker method (Dekker, 1969) was used to numerically solve for volume given pressure and temperature. The implemented code was modified from Withers (2017).

^e For blueschists, boudin spacing δ is used instead of d , and is set at 100 μm .

^f Wet olivine fugacity (C_{OH}) was set to 600 MPa (Hirth & Kohlstedt, 2003).